Electronic Supplementary Material (ESI) for Physical Chemistry Chemical Physics

Supporting Information

Stability, surface features, and atom leaching of palladium nanoparticles: toward prediction of catalytic functionality

Hadi Ramezani-Dakhel[1], Peter A. Mirau[2], Rajesh R. Naik[2], Marc R. Knecht[3],
Hendrik Heinz[1]*

[1]University of Akron, Department of Polymer Engineering, Akron, Ohio, 44325, USA.

[2]Wright-Patterson Air Force Base, Nanostructured and Biological Materials Branch, Air Force Research Laboratory, Dayton, Ohio, 45433, USA.

[3]University of Miami, Department of Chemistry, Coral Gables, Florida, 33146, USA.

* Corresponding author: hendrik.heinz@uakron.edu

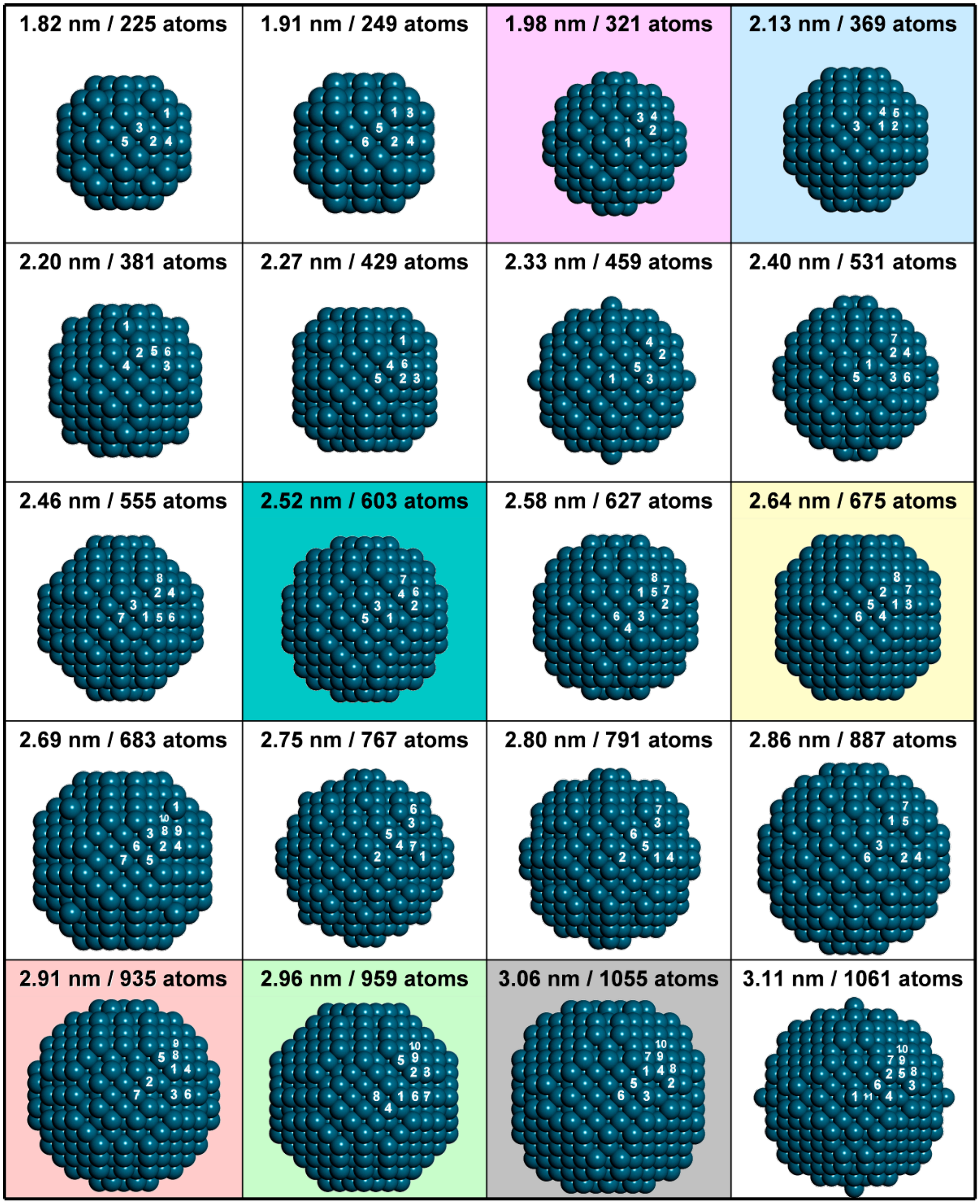

Fig. S1. Surface features of near-spherical Pd particles of 1.8 nm to 3.1 nm size. All chemically distinct atom types on the surface are identified and numbered in the order of increasing abstraction energy. Background color highlights energetically stable particles.

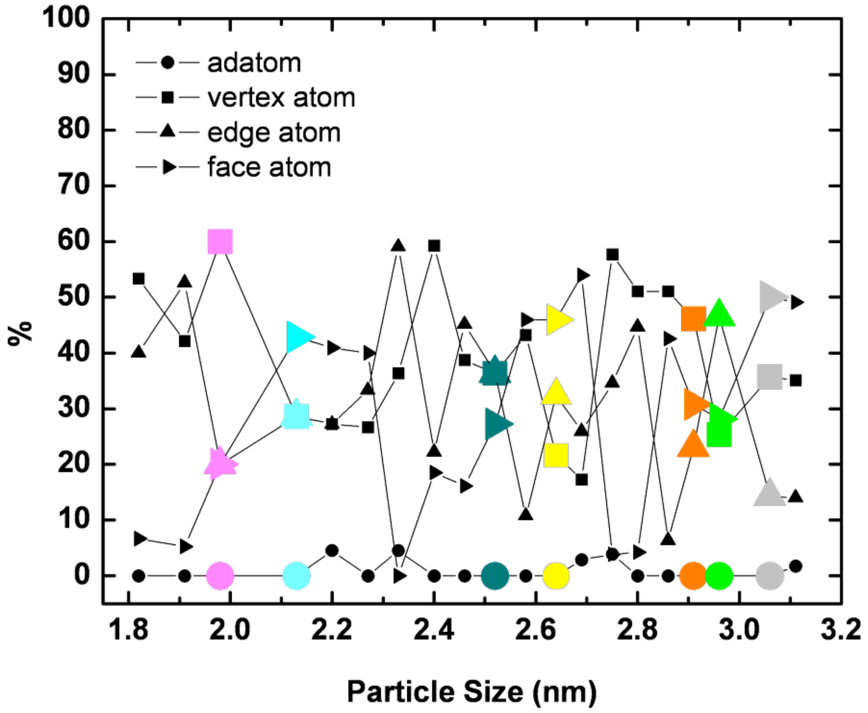

Fig. S2. Percentage of adatoms, vertex, edge, and face atoms on the nanoparticle surface as a function of particle size. Colored symbols correspond to stable particles (Fig. S1) and black symbols represent less stable and unstable particles.

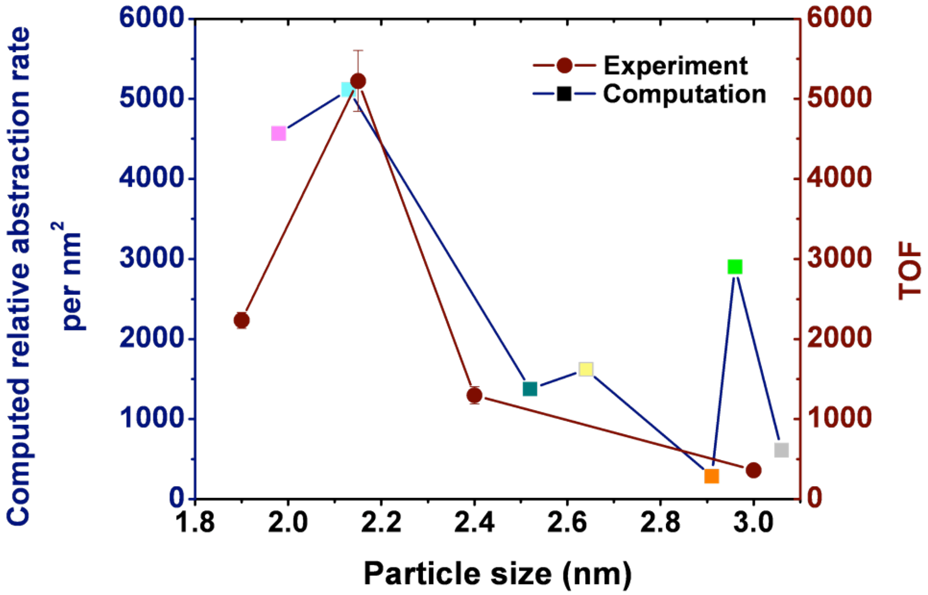

Fig. S3. Correlation of the computed leaching rate of bare palladium nanoaprticles normalized to the surface area of the particles with the measured catalytic turnover frequencies in Stille reactions as a function of nanoparticle size (TOF data from ref S1).

Table S1. Abstraction energies and number of equivalent atoms on the particle surface for each atom type calculated with the CHARMM-METAL force field. The numbering of atom types (1, 2, 3, …) corresponds to Fig. S1.

Size (nm)	**# of atoms**	**Abstraction energy (kcal/mol) for each atom type # of equivalent atoms**										
		1 #	**2 #**	**3 #**	**4 #**	**5 #**	**6 #**	**7 #**	**8 #**	**9 #**	**10 #**	**11 #**
1.825	225	38.66 24	43.10 24	50.66 24	51.55 12	58.98 6						
1.906	249	38.35 24	46.90 24	48.80 24	54.08 12	55.87 24	60.16 6					
1.984	321	**43.87** **24**	**46.87** **48**	51.00 24	60.85 24							
2.131	369	**44.15** **48**	51.40 48	57.77 24	61.04 24	62.94 24						
2.201	381	38.01 8	44.83 48	56.17 48	58.98 24	61.60 24	63.70 24					
2.268	429	39.34 24	42.07 24	48.15 12	50.74 48	60.30 24	64.20 48					
2.334	459	32.63 6	40.03 24	43.51 24	49.47 24	52.20 54						
2.398	531	41.20 24	45.0 48	48.90 24	51.10 24	52.0 6	54.70 12	60.90 24				
2.460	555	43.78 24	45.78 48	50.93 24	51.30 24	53.76 24	55.34 12	59.14 6	61.07 24			
2.521	603	**44.90** **24**	**45.01** **48**	51.42 24	51.71 48	59.39 6	61.23 24	63.05 24				
2.580	627	40.13 24	45.75 48	48.50 24	56.47 24	56.52 48	60.49 6	61.82 24	63.79 24			
2.638	675	**44.59** **48**	49.94 24	51.55 48	58.35 24	60.70 24	61.64 6	63.29 24	64.56 24			
2.695	683	30.10 8	44.65 48	50.03 24	51.70 48	58.37 24	60.72 24	61.66 6	62.764 8	65.07 24	69.30 24	
2.751	767	38.83 8	44.03 24	45.52 48	47.05 48	52.86 24	58.63 8	59.26 48				
2.805	791	42.38 24	44.24 24	45.76 48	48.31 12	51.87 48	53.43 24	58.74 8				
2.859	887	41.74 48	45.31 24	45.86 24	52.35 12	56.10 48	58.27 24	62.50 8				
2.911	935	**45.57** **48**	**46.71** **48**	49.08 24	51.33 24	51.37 24	54.84 12	58.46 24	62.22 48	64.18 8		
2.963	959	**43.68** **24**	**46.22** **48**	51.51 24	51.67 48	51.75 24	53.86 24	55.40 12	60.56 24	62.31 48	64.23 8	
3.063	1055	**45.15** **48**	**45.84** **48**	48.88 24	57.24 48	58.76 48	61.59 24	61.91 24	61.99 24	64.35 24	64.91 24	
3.112	1061	33.13 6	45.21 48	45.85 48	49.03 24	57.25 48	59.37 48	61.92 24	62.00 24	64.35 24	64.92 24	66.32 24

S1. Details of Computational and Analysis Procedures

S1.1. Models. Models of elemental palladium in all atomic resolution up to 8×8×8 multiples of the unit cell were prepared from the crystal structure according to X-Ray data.[S2] Models of the near-spherical nanoparticles were then obtained by selection of an atom near the center and application of a spherical cutoff. The initial cutoff was 0.9 nm (9 Å), leading to particles of ~1.8 nm size and then increased in steps of 0.01 nm (0.1 Å) to obtain particles up to ~3.1 nm size. The crude nanoparticles were subjected to molecular dynamics simulation for more than 5 ns at room temperature as well as at higher temperatures up to 800 K to test the stability. Particles with adatoms and incomplete facets showed surface reconstruction, although the ratio of surface facets remained similar. The core of all particles remained the same at room temperature and upon annealing.

The reported size of the particles corresponds to the line connecting two outermost atoms and crossing the center of the particle, similar to measurements on TEM images. The graphical interface of Materials Studio was employed in the preparation of the models.[S3]

S1.2. Force Field. We employed thermodynamically consistent Lennard-Jones (LJ) parameters for fcc metals for all calculations as implemented in the CHARMM-METAL force field.[S4,S5] These LJ parameters are known since 2008 and reproduce experimental measurements of densities and surface energies of fcc metals at 298 K, following the principle of thermodynamic consistency.[S4] The parameters eliminate common deviations in computed bulk and surface properties by several hundred percent in comparison to experiment by alternative potentials and have turned LJ potentials into well-performing models for fcc metals under standard conditions.

The simulation of bulk, surface, and interface properties of fcc metals in aqueous media has been demonstrated in very good agreement with a wide range of experimental data.[S4-S8] These data include (1) the density of the metals (0.1 %), (2) the surface tension (5%), (3) the anisotropy of metal surface energies ({111} vs. {100}, {111} vs. {110}) within experimental uncertainty, (4) metal-water interface tensions (10%)[S4], (5) water layering and the decrease in dielectric constant of water in the first three molecular layers (78, 32, 6 on gold) towards the metal surface (10%),[S6] (6) relative adsorption energies of 20 amino acids in water on Au {111} surfaces,[S7] (7) adsorption energies of peptides on different Au and Pd facets,[S8] (8) correct trends in adsorption of peptides on nanostructured metal surfaces of different shapes,[S5] (9) consistency with quantum-mechanical results for smaller subsystems,[S8] and (10) properties of Au-Pt alloys.[S9] Experimental support for the reliability of the model thus includes measurements of surface tensions, measurements of peptides binding constants, the relative affinity of amino acids in phage display, the distinction of facets for binding, similarities in peptide binding strength to similar fcc metals, observations of shape control, and the properties of Au-Pt alloys.[S4-S9] Notably also computed bulk, shear, and Young's moduli of Pd metal deviate less than 5% from measurements. Limitations include the neglect of electronic structure, the difficulty to simulate chemical reactions, and the neglect of contributions by induced charges to adsorption.[S6]

S1.3. Simulation Protocol. Molecular dynamics simulations of the nanoparticles before and after atom abstraction were carried out using the Discover program for shorter simulations[S3] and the NAMD program for longer simulations.[S10] We employed the NVT ensemble, the velocity Verlet integrator, a time step of 1 fs, and summation of van-der-Waals interactions using a spherical cutoff at 1.2 nm. Single point energies were computed using the Discover program.

Test calculations of the nanoparticles before and after atom abstraction in aqueous solution were carried out using the NAMD program.

S1.4. Calculation of the Cohesive Energy. The cohesive energy of the near-spherical Pd nanoparticles was calculated to evaluate the relative energetic stability. We performed molecular dynamics simulations of the nanoparticles for a duration of 5 ns and then subtracted the average energy from the average energy of isolated palladium atoms in the gas phase (zero according to the CHARMM-METAL force field). The cohesive energy was then plotted as a function of particle size to approximate a master curve as well as offsets for individual particles due to the discrete number of atoms and deviation from perfect spherical shape (Fig. 1b). Comparisons to DFT calculations and experimental data are presented in section S2.

S1.5. Determination of Surface Composition by {h k l} Facets. Percentages of the bounding facets of each particle were calculated upon analysis of the 3D geometry. The total surface area was partitioned into portions covered by {111}, {100}, and {110} facets and percentages of these areas are reported (Fig. 2). Some particles contain adatoms that cover a small portion of the surface area (<3%). For simplicity, we subtracted this area from the total area of the respective host facet and excluded this area from the total so that the sum of percentages of {111}, {100}, and {110} facets still accounts for 100%. We also examined the percentages of adatoms, vertex, edge, and face atoms on the surface of each nanoparticle by number counts (Fig. S2).

S1.6. Calculation of Atom Abstraction Energy. Abstraction energies of equivalent atoms were calculated by detachment of individual atoms from the surface of the particles to a distance of at least 1.2 nm. The abstraction energy was obtained as a difference in total energy of the system in the detached and bound states using single point energies. Molecular dynamics simulations in the abstracted states sometimes lead to surface reconstruction by filling vacant positions with the neighbor atoms. This scenario was observed when atoms of higher abstraction energies were detached from the surface next to atoms with lower abstraction energy. For example, once atom 4 in the particle with 321 atoms (Fig. 3) was detached, subsequently atom 2 filled its position within 2 ns simulation time. Faster rearrangement of atoms on the surface (within 20 ps) was also found for test simulation of abstraction in aqueous environment. The abstraction energies were found to be similar, however.

S1.7. Computation of Relative Leaching Rate. The overall rate of atom abstraction for a given nanoparticle was computed using the abstraction energies of all individual atoms i that constitute the surface. We assume that the probability $P(i)$ for the abstraction of an atom i is $P(i) = C \cdot e^{-\frac{E_i}{RT}}$ where C is a constant and E_i is the abstraction energy. We further assume that probabilities of abstraction of the different surface atoms $i = 1, 2, ..., N_S$ are additive, justified by their small order of magnitude. Therefore, the estimated relative rate of abstraction R for a particle of a given size is then given as a summation over all individual surface atoms i and normalized to the total number of Pd atoms N that constitute the particle:

$$R_N = \frac{C}{N} \sum_{i=1}^{N_S} e^{-\frac{E_i}{RT}} \tag{S1}$$

$$R_N = \frac{1}{N} \sum_{i=1}^{N_S} e^{-\frac{E_i - 50.4\,kcal/mol}{RT}} \tag{S2}$$

Normalization to the total number of atoms enables comparisons to measurements of reaction rates, in which the turnover frequency (TOF) is determined as rate of formation of the product divided by the concentration of catalyst in moles of Pd atoms per liter.[S1] From equation (S1) to equation (S2), we reformulate the constant C using an offset in energy of 50.4 kcal/mol in the exponential, which yields reaction rates that can be easily compared with measurements (Fig. 4a). Alternative to the rate of abstraction per total number of atoms R_N, the rate of abstraction can also be normalized to the surface area *A* of the particle, which allows comparisons of surface performance and excludes inert atoms inside the particle core:

$$R_A = \frac{1}{A}\sum_{i=1}^{N} e^{-\frac{E_i - 48.5 kcal/mol}{RT}} . \tag{S3}$$

Equation (S3) similarly yields reaction rates that can be easily compared to measurements. The surface area *A* of the nanoparticle is given in square nanometers, and abstraction rates R_A are normalized per surface area (Fig. S3).

The abstraction rate can also be obtained in a convenient equivalent way, in which the summation runs over all atom types $j = 1, 2, ..., K$ instead of running over all individual atoms *i*. For each atom of the same type *j*, a certain number of equivalent atoms N_j are found on the surface, which share the same abstraction energy E_j. We can then express the probability $P(j)$ for the abstraction of an atom of type *j* as $P(j) = C \cdot N \cdot e^{-\frac{E_j}{RT}}$ where *C* is the same constant as in equation (S1), N_j is the number of equivalent atoms of type *j*, and E_j is the corresponding abstraction energy. The estimated relative rate of abstraction *R* normalized by the total number of atoms *N* in the particle (or the surface area *A*) then is:

$$R_N = \frac{1}{N}\sum_{j=1}^{K} CN_j e^{-\frac{E_j}{RT}} \tag{S4}$$

$$R_N = \frac{1}{N}\sum_{j=1}^{K} N_j e^{-\frac{E_j - 50.4 kcal/mol}{RT}} \tag{S5}$$

$$R_A = \frac{1}{A}\sum_{j=1}^{K} N_j e^{-\frac{E_j - 48.5\ kcal/mol}{RT}} \quad . \tag{S6}$$

The advantage is that the summation needs to include only the first one or two atom types ($j = 1, 2$), as the increase in abstraction energies toward higher order atom types is so large (>5 RT) that contributions to the abstraction rate are essentially zero (Fig. 3 and Table S1). Therefore, significant contributions to the leaching rate depend on the abstraction energies of atoms of type 1 and the number of equivalent surface atoms of type 1, possibly plus the abstraction energy of atoms of type 2 and the number of equivalent surface atoms of type 2. Accordingly, only the highlighted values of E_j and N_j in boldface in Fig. 3c and in Table S1 need consideration in the computation of abstraction rates while atom types with higher values E_j have a negligible effect. Equations (S4), (S5), and (S6) are equivalent to equations (S1), (S2), and (S3).

In the case of partial atom abstraction, the abstraction energy does not significantly decrease. For example, a required separation of only 3 Å instead of 12 Å decrease the abstraction less than one third, i.e., over 30 kcal/mol if the energy upon full separation was 44 kcal/mol. Incomplete abstraction would be interesting to examine in more detail in future work. It may be possible that atoms up to type 3 and higher contribute to the leaching rate by direct abstraction or concerted movement to the positions being vacated on the surface.

S2. Comparison of Nanoparticle Structure and Cohesive Energy to DFT Calculations and Experiment

Previous DFT calculations examined the structure and energy of small palladium clusters up to nanoparticles of 309 atoms size.[S11] Small atomic clusters were investigated at temperatures of 50

K and reported to be floppy. Larger clusters of Pd-231 and Pd-309 were investigated at 100 K and assumed to be octahedral.[S11] Regular shapes below 150 atoms (~1.5 nm) size could not be observed in experiment at room temperature and earlier molecular dynamics simulations using CHARMM-METAL have shown amorphous shapes below 1.0-1.5 nm size at room temperature, followed by a transition to crystalline particles for larger size.[S12] Therefore, we concentrate on particles larger than 150 atoms. Synthesized nanoparticles are near-spherical unless highly facet-specific capping agents are used,[S1, S13] and thus different from octahedra suggested by DFT calculations.[S11]

The octahedra with 231 and 309 atoms in DFT calculations at 100 K exhibit a cohesive energy of 70.7 and 71.7 kcal/mol.[S11] The cohesive energy was possibly overestimated by 30% relative to measurements as indicated by comparisons for a Pd_2 cluster. Near-spherical nanoparticles with 249 and 321 atoms in molecular dynamics simulations at 298 K exhibited a cohesive energy of only 36.2 and 37.6 kcal/mol (Fig. 1b). Values from both DFT and from force field are less than the cohesive energy of bulk Pd of 90.3 kcal/mol according to measurements.[S2] As nanoparticles are only slightly bigger than the range of interatomic-interactions (~1 nm) they are expected to exhibit lower cohesive energies compared to bulk metal.[S5] Hereby, DFT results likely overestimate and force field results likely underestimate the true cohesive energy. A systematic underestimate of cohesive energies, i.e., vaporization energies, of Pd using the force field is associated with a temperature range of 298 ± 200 K for the optimization of parameters while much higher temperatures over 3236 K are required to vaporize palladium into atoms.[S4] The underestimate of cohesion at room temperature is accompanied, however, by very close agreement of surface energies and surface energy anisotropies for different {h k l} facets with measurements (<5% deviation).[S4]

S3. Mechanistic Aspects and Individual Steps in Stille Coupling Reactions

Numerous studies have established mechanistic aspects of carbon-carbon coupling reactions in solution using homogeneous organo-palladium complexes such as $Pd(PPh_3)_2Cl_2$.[S14-S16] Coupling reactions using metal nanoparticles as catalysts, in contrast, are still not as well understood as they involve two different phases of solid nanoparticles and of the reactant solution. The reaction mechanism therefore differs from that using organo-palladium complexes (Fig. 4b).[S17-S19]

S3.1. Reaction Overview. The Stille coupling reaction using metal nanoparticles involves the oxidative addition of an aryl halide Ar−X to a Pd atom on the nanoparticle surface as a first step (Fig. 4b). This Pd atom is then likely abstracted from its original position as an organometallic Pd^{II} compound Ar–Pd–X. The next major step in the reaction mechanism is transmetalation in which an organotin ($PhSnCl_3$) reacts with the Ar−Pd−X compound to form Ar−Pd−Ph and a tin(IV) species. The final step of the reaction involves the reductive elimination of Ar−Ph with the release of a Pd^0 atom that likely returns to the particle surface or continues through an additional Stille coupling cycle should sufficient aryl halide remain in solution (Fig. 4b).[S20] Contributions of individual steps to the overall reaction rate are discussed in the following.

S3.2. Oxidative Addition. The rate of the Stille reaction using dissolved organopalladium complexes and the same organotin complex has shown a dependence on the type of aryl halide, such as lower reaction rates for aryl chloride and higher rates for aryl bromide and iodide.[S14, S15] These observations indicate that oxidative addition may participate as a rate-determining process. In case of solid Pd nanoparticles as a catalyst, a different set of factors may affect the rate of oxidative addition (first step in Fig. 4b). The availability of Pd surface atoms is also limited through the coordination of ligands onto the particle surface, facet specific binding, and surface coverage. The rate of oxidative addition may thus be additionally affected by the nanoparticle-ligand combination, the type of reactants, and reaction conditions, potentially slowing down the reaction rate to be the controlling step.

S3.3. Atom Leaching. Ultimately, also atom leaching is required. The abstraction of palladium atoms from the nanoparticle surface to the solution appears to be a key step in the kinetic pathway of coupling reactions using palladium nanoparticles (second step in Fig. 4b).[S1, S21-S23] Several studies have shown that variations in particle size using similar ligands and reaction conditions lead to different catalytic turnover frequencies.[S1, S24, S25] As we have shown here (Fig. 3 and Table S1), the significant energy barrier for atom abstraction as well as the surface coverage of the particles by ligands may cause atom abstraction to be slower than other steps and determine the overall reaction rate. Different reactivity of particles of different sizes with similar binding ligands under the same reaction conditions can be explained using atom abstraction energies (Fig. 4a). This trend is also consistent with a correlation between the concentration of free palladium atoms in solution and the rate of the reaction.[S23]\

S3.4. Transmetalation. The transmetalation step has often been found to be the rate determining step using organopalladium catalysts in solution as the accumulation of intermediates upon oxidative addition such as $PdL_m(Ar)(X)$ was observed.[S14] Information about the rate of transmetalation using nanoparticle catalysts is currently scarce (third step in Fig. 4b). We observed in the course of Suzuki coupling that a change in transmetalation agent from organotin to organoboron compounds affects the reaction rate (details to be reported elsewhere). Therefore, transmetalation could be involved as a rate-determining step.

S3.5. Reductive Elimination. The last step in the reaction is the reductive elimination of the newly formed organic compound (fourth step in Fig. 4b). The reductive elimination is the key bond-forming step in carbon-carbon coupling reactions and has been found to control the rate of reaction in some instances.[S14, S26]

Supplementary References

S1. R. Coppage, J. M. Slocik, M. Sethi, D. B. Pacardo, R. R. Naik and M. R. Knecht, *Angew Chem Int Edit*, 2010, **49**, 3767-3770.

S2. D. R. Lide, *CRC Handbook of chemistry and physics : a ready-reference book of chemical and physical data, 83rd ed., by David R. Lide.* Boca Raton: CRC Press, 2002.

S3. Materials Studio program, version 6.0 (Accelrys Inc., CA, 2012).

S4. H. Heinz, R. A. Vaia, B. L. Farmer and R. R. Naik, *J Phys Chem C*, 2008, **112**, 17281-17290.

S5. J. Feng, J. M. Slocik, M. Sarikaya, R. R. Naik, B. L. Farmer and H. Heinz, *Small*, 2012, **8**, 1049-1059.

S6. H. Heinz, K. C. Jha, J. Luettmer-Strathmann, B. L. Farmer and R. R. Naik, *J R Soc Interface*, 2011, **8**, 220-232.

S7. J. Feng, R. B. Pandey, R. J. Berry, B. L. Farmer, R. R. Naik and H. Heinz, *Soft Matter*, 2011, **7**, 2113-2120.

S8. H. Heinz, B. L. Farmer, R. B. Pandey, J. M. Slocik, S. S. Patnaik, R. Pachter and R. R. Naik, *J Am Chem Soc*, 2009, **131**, 9704-9714.

S9. V. Petkov, B. N. Wanjala, R. Loukrakpam, J. Luo, L. F. Yang, C. J. Zhong and S. Shastri, *Nano Lett*, 2012, **12**, 4289-4299.

S10. J. C. Phillips, R. Braun, W. Wang, J. Gumbart, E. Tajkhorshid, E. Villa, C. Chipot, R. D. Skeel, L. Kale and K. Schulten, *J Comput Chem*, 2005, **26**, 1781-1802.

S11. P. Nava, M. Sierka and R. Ahlrichs, *Phys Chem Chem Phys*, 2003, **5**, 3372-3381.

S12. R. Coppage, J. M. Slocik, B. D. Briggs, A. I. Frenkel, H. Heinz, R. R. Naik and M. R. Knecht, *J Am Chem Soc*, 2011, **133**, 12346-12349.

S13. B. Lim, M. J. Jiang, J. Tao, P. H. C. Camargo, Y. M. Zhu and Y. N. Xia, *Adv Funct Mater*, 2009, **19**, 189-200.

S14. A. d. Meijere and F. o. Diederich, *Metal-catalyzed cross-coupling reactions*, Wiley-VCH, Weinheim, 2004.

S15. P. Espinet and A. M. Echavarren, *Angew Chem Int Edit*, 2004, **43**, 4704-4734.

S16. K. C. Nicolaou, P. G. Bulger and D. Sarlah, *Angew Chem Int Edit*, 2005, **44**, 4442-4489.

S17. D. Astruc, *Nanoparticles and catalysis*, Wiley-VCH, Weinheim, 2008.

S18. M. Bernechea, E. de Jesus, C. Lopez-Mardomingo and P. Terreros, *Inorg Chem*, 2009, **48**, 4491-4496.

S19. N. T. S. Phan, M. Van Der Sluys and C. W. Jones, *Adv Synth Catal*, 2006, **348**, 609-679.

S20. R. Narayanan, C. Tabor and M. A. El-Sayed, *Top Catal*, 2008, **48**, 60-74.

S21. A. K. Diallo, C. Ornelas, L. Salmon, J. R. Aranzaes and D. Astruc, *Angew Chem Int Edit*, 2007, **46**, 8644-8648.

S22. D. B. Pacardo, J. M. Slocik, K. C. Kirk, R. R. Naik and M. R. Knecht, *Nanoscale*, 2011, **3**, 2194-2201.

S23. S. S. Prockl, W. Kleist, M. A. Gruber and K. Kohler, *Angew Chem Int Edit*, 2004, **43**, 1881-1882.

S24. J. Le Bars, U. Specht, J. S. Bradley and D. G. Blackmond, *Langmuir*, 1999, **15**, 7621-7625.

S25. M. Perez-Lorenzo, *J Phys Chem Lett*, 2012, **3**, 167-174.

S26. A. L. Casado, P. Espinet, A. M. Gallego and J. M. Martinez-Ilarduya, *Chem Commun*, 2001, 339-340.